PCCP

PAPER

View Article Online
View Journal | View Issue

Cite this: *Phys. Chem. Chem. Phys.*, 2018, **20**, 23363

On-surface self-assembly of tetratopic molecular building blocks†

Damian Nieckarz,[a] Wojciech Rżysko[b] and Paweł Szabelski *[a]

Received 15th June 2018,
Accepted 24th August 2018

DOI: 10.1039/c8cp03820a

rsc.li/pccp

Self-assembly of functional molecules on solid substrates has recently attracted special attention as a versatile method for the fabrication of low dimensional nanostructures with tailorable properties. In this contribution, using theoretical modeling, we demonstrate how the architecture of 2D molecular assemblies can be predicted based on the individual properties of elementary building blocks at play. To that end a model star-shaped tetratopic molecule is used and its self-assembly on a (111) surface is simulated using the lattice Monte Carlo method. Several test cases are studied in which the molecule bears terminal arm centers providing interactions with differently encoded directionality. Our theoretical results show that manipulation of the interaction directions can be an effective way to direct the self-assembly towards extended periodic superstructures (2D crystals) as well as to create assemblies characterized by a lower degree of order, including glassy overlayers and quasi one-dimensional molecular connections. The obtained structures are described and classified with respect to their main geometric parameters. A small library of the tetratopic molecules and the corresponding superstructures is provided to categorize the structure–property relationship in the modeled systems. The results of our simulations can be helpful to 2D crystal engineering and surface-confined polymerization techniques as they give hints on how to functionalize tetrapod organic building blocks which would be able to create superstructures with predefined spatial organization and range of order.

1. Introduction

Molecular self-assembly on solid surfaces has been one of the most intensively studied topics in surface science and nanotechnology recently. The growing interest in the fabrication of low dimensional structures on solid supports originates mainly from enhanced possibilities of controlling intermolecular interactions/bonding which are offered by the reduced configurational freedom of adsorbed molecules, as compared to the bulk phase. The resulting ordered 2D structures formed by functional building blocks on graphite or metallic substrates[1,2] have been recognized as versatile platforms for controlled (periodic) spatial positioning of atoms and molecules with diverse electronic, magnetic or catalytic properties.[3–5] These functional units can be either included in the adsorbed superstructure directly, as in the case of, for example, porphyrins and phthalocyanines,[6,7] and they can form porous networks,[8,9] nanovoids of which can be next filled with foreign matter with presumed physicochemical activity.[10,11] In both cases, 2D molecular matrices are readily obtainable and their intrinsic properties can be precisely tuned by a suitable choice of the building block at play. This beneficial property has been demonstrated in numerous experimental studies in which organic building blocks with linear[12,13] and star-shaped[8–11] backbones have been used to create extended adsorbed patterns, usually imaged with Scanning Tunneling Microscopy (STM). In these cases often openwork on-surface structures with rhombic,[14] square,[15] rectangular[16] and hexagonal[9] void spaces have been created by means of appropriately designed building blocks. The interactions sustaining these porous superstructures can be of different nature ranging from hydrogen-bonding,[17] metal–ligand coordination in mixed metal–organic systems,[12] halogen bonding[18] to even van der Waals type.[9]

Among different building blocks used to create nanoporous networks on solid surfaces star-shaped organic molecules equipped with three and four arms have been most prevalent in the experiment, including tricarboxylic acids,[19–21] dehydrobenzoannulene (DBA) derivatives with long alkyl chain arms[9,22] and tripod- and cross-shaped molecules functionalized with pyridyl groups.[17,23–26] These tectons, due to ramified geometry, facilitate greatly the formation of pores whose rims comprise interacting molecular arms. Moreover, when the terminal active centers of the star-shaped organic molecules are equipped with halogen atoms, these units can be used as monomers of the surface-assisted

---

[a] Department of Theoretical Chemistry, Maria-Curie Skłodowska University, Pl. M.C. Skłodowskiej 3, 20-031 Lublin, Poland. E-mail: szabla@vega.umcs.lublin.pl; Fax: +48 081 537 56 85; Tel: +48 081 537 56 20

[b] Department for the Modeling of Physico-Chemical Processes, Maria-Curie Skłodowska University, Pl. M.C. Skłodowskiej 3, 20-031 Lublin, Poland

† Electronic supplementary information (ESI) available. See DOI: 10.1039/c8cp03820a

Ullmann polymerization. This method of fabrication of diverse low-dimensional covalently bonded organic polymers has recently attracted great attention as a promising route to graphitic materials, for example graphene networks, flakes and nanoribbons.[27–29]

From the experimental studies on the directed self-assembly of functional organic molecules on solid surfaces it follows that often a small change in the intrinsic properties of the building block results in 2D superstructures with totally different morphologies. A telling example is the metal–organic self-assembly of straight and bent polyphenyl rods terminated with nitrile groups which results in hexagonal porous networks[30] and Sierpiński triangle fractals,[31] respectively. A similar conclusion refers to tripod shaped molecules such as DBAs for which, depending on the molecular aspect ratio, chiral porous polymorphs differing in pore shape can be obtained.[22] Another factor that is crucial for the structure formation in adsorbed overlayers is the intramolecular distribution of active centers providing interactions cementing the resulting superstructures. For example, this molecular property has been demonstrated to affect strongly the outcome of 2D self-assembly of 1,3,5-tris(pyridin-4-ylethynyl)benzene (TPyB) – a tripod building block bearing terminal pyridyl groups with N atoms in the *meta* position.[24] Due to the rotatability of the pyridyl groups of *meta*-TPyB different surface conformers have been found on the surface, leading to much more complex H-bonded structures, as compared with those formed by the analogous molecule with N atoms in the *para* position. A similar effect has been observed recently in the on-surface Ullmann type polymerization of the brominated tripod unit 1,3,5-tris(3-bromophenyl)benzene (*m*TBPB) on Ag(111).[32] For this tecton, the rotatability of the *meta*-halogenated benzene rings resulted in covalently bonded porous nanoribbons and nanodots whose formation was preceded by diverse molecular precursor architectures including halogen-bonded networks and organo-metallic chains.

The insights from the 2D self-assembly of functional tripod building blocks demonstrate that manipulating intramolecular distribution of interaction centers, thus directionality of intermolecular interactions, is an effective method to direct the assembly process toward structures with preprogrammed geometry and functions. While this strategy has been used for various tripod tectons,[21,24,32,33] analogous experimental studies on more ramified functional building blocks, including tetrapod units, have focused mainly on molecules with cross-shaped backbones, including derivatized porphyrins and phthalocyanines. In these instances, molecular arms have usually comprised terminal pyridyl[25,26,34,35] and/or cyano[36] groups and also halogen atoms[37,38] attached in a way enabling the creation of metal-mediated intermolecular links involving collinear arms of neighboring molecules. A similar geometric principle, based on the collinearity of interacting functional arms, has been applied to ⟩–⟨-shaped tetracarboxylic acids[39,40] and to halogenated polyaromatic tectons[41,42] adsorbed on solid substrates. Even though this simple approach has been very useful from a practical point of view, often resulting in extended porous networks, it is certainly not the only possible way of encoding intermolecular interactions to create surface-confined supramolecular constructs comprising tetrapods with functional arms. In real situations, however, to examine the effect of directionality of the encoded molecule–molecule interactions on the morphology of the corresponding 2D assemblies a series of test building blocks is needed, differing in the number and position of active centers. As the synthesis of such probe tectons can be time and resource consuming alternative strategies based on theoretical methods have been recently proposed.

Computer simulations of molecular assemblies have been an efficient and robust theoretical tool for predicting structure formation in adsorbed systems comprising a large number of functional organic molecules. Among them calculations with the Molecular Dynamics[43–45] and Monte Carlo (MC)[46–49] methods have been most prevalent, resulting in good matches with the experiment. In this field, MC calculations based on the coarse-grained representation of real systems have been particularly useful, as they are computationally less expensive and allow for modeling of molecular systems with a minimal number of adjustable parameters. Moreover, with this approach it is possible to develop general models in which molecular building blocks represent a certain class of chemically different structures whose common feature is, for example, shape and interaction pattern. This type of modeling has been recently successfully used in the case of cross-shaped molecules[48–51] and molecular tripods equipped with differently distributed interaction centers.[17,23,47,52] In particular, in our previous MC studies we demonstrated that properly encoded directionality of intermolecular interactions can be used to direct the on-surface self-assembly of simple tripod building blocks into superstructures with diverse architectures, including networks, strings, ladders and other molecular connections.[52] As these results were in good agreement with the literature data and predicted new structures whose formation was later confirmed experimentally (*m*TBPB strings[32]) in this work we extend our approach to more complex building blocks equipped with four arms. To that end we examine the 2D self-assembly of ⟩–⟨-shaped tetrapod tectons bearing terminal active centers providing intermolecular interactions with adjustable directionality. Our main objective is to identify and categorize possible structures formed by these building blocks differing in the assignment of interaction directions. The structure–property relationship found in this study can be helpful in the preliminary screening of molecular libraries aiming at selection of a functional tetrapod building block able to create adsorbed structures with preprogrammed morphology.

2. The model and simulations

To model the self-assembly of tetratopic molecules with differently assigned interactions we adopted the coarse grained approach[17,22,23,51,52] in which the molecular backbone consisted of six segments arranged in the shape shown in Fig. 1. This tecton was assumed to be rigid and planar, so that each composite segment occupied one vertex (adsorption site) on a triangular lattice composed of equivalent adsorption sites (see Fig. 1). The arm segments of the tetrapod provided differently encoded directional interactions which are schematically shown by the arrows in the figure. Accordingly, the molecules were able to

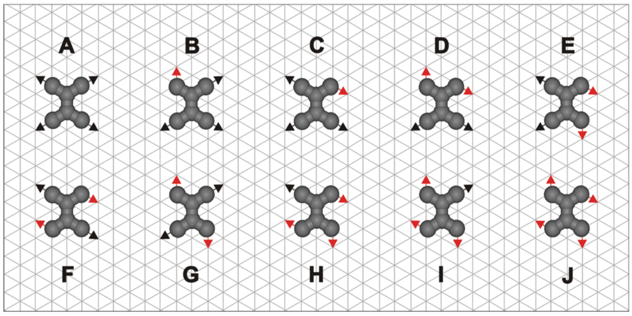

Fig. 1 Schematic representation of the model tectons **A–J** adsorbed on a triangular lattice and used in the simulations. The arrows pointing away from the arm segments indicate the interaction directions assumed for each tecton. The arrows colored in red show the interaction directions which are different from those encoded in the parent molecule **A**. For the chiral units (**B–J**) only one surface enantiomer, called arbitrarily *R*, is shown for clarity.

interact only when their arm segments occupied adjacent sites on the lattice and, additionally, when the corresponding interaction directions were collinear (→ ←).

In such a case, the segment–segment interaction energy was equal to ε, which is an adjustable model parameter. For the remaining configurations this energy was assumed to be zero. Similarly, because of the energetic homogeneity of the surface, the molecule–surface interactions were neglected in our model. Note that the molecules **B–J** can adopt two mirror-image adsorbed configurations with respect to the assigned interaction directions and thus they are chiral in 2D. Consequently, for each tecton these configurations were arbitrarily called *R* (shown in Fig. 1) and *S*. In the following, the term enantiopure refers to adsorbed systems comprising exclusively *R*- or *S*-enantiomers of **B–J** shown in Fig. 1.

Regarding the correspondence between our model and real molecular systems, the following examples can be adduced. The simplified model described above can represent such structurally similar molecules as tetracarboxylic acids whose functional –COOH groups pointing out from a linear, usually a (poly)aromatic, core provide intermolecular hydrogen bonding.[39,40] For these tectons, the directional interactions of our model can correspond to the hydrogen bonds formed between differently positioned carboxylic groups. Another example is represented by the tetrapod polyaromatic units bearing halogen atoms linked to the outer phenyl rings.[41,42] Molecules of this functionality are frequently used in the on-surface polymerization reactions in which directionality of the resulting covalent bonds is determined by the position (usually *para* or *meta*) of halogen atoms (X = Br or I). In these reactions the precursor two-coordinate molecule–X–metal–X–molecule links are usually linear and aligned according to the directionality of the contributing X–molecule bonds. In this view, without explicit metal atom modeling, the proposed model can also describe the formation of metal–organic precursors whose structure is often inherited by the corresponding 2D covalent polymers. Very recently, tetrapods resembling the tecton **A** and equipped with terminal aldehyde groups have been used to create bicomponent covalent networks at the graphite/liquid phase interface.[53] In this case, the formyl-functionalized arms were covalently linked with the mediating ditopic rod-shaped amine molecules to produce different surface polymorphs. The connectivity of the resulting superstructures was solely determined by the position of the aldehyde groups in the tetrapod building block, highlighting the correspondence between this structural property and the interaction directionality considered in our model.

To trace the self-assembly of the tectons **A–J** we used the Monte Carlo simulation technique in the canonical ensemble.[52] Most of the calculations were performed on a rhombic fragment of a triangular lattice with linear size L equal to 200 sites. In some cases larger lattices with $L = 480$ were also used to study coexistence of different molecular patterns. The basic MC simulation scheme can be outlined as follows. In the first step N molecules of a given type (**A–J**) were randomly distributed on the lattice at a fixed temperature T. For the chiral units (**B–J**), two situations were considered, including enantiopure systems comprising $N = N_R$ molecules from Fig. 1 (*R*-enantiomers) and racemic overlayers with $N = N_R + N_S$ where N_S denotes the number of molecules with *S*-handedness and $N_R = N_S$. Next, the adsorbed phase was equilibrated in a series of MC steps, each of which involved random translation and rotation of a molecule. To that purpose a molecule was selected at random and its potential energy in the current position, U_{old}, was calculated by summing the directional (→ ←) interactions with neighboring molecules. If occurring, each directional interaction contributed to U_{old} with ε. The selected molecule was next moved to a new position on the lattice. In this case, a cluster of adsorption sites matching the shape of **A–J** was randomly chosen. If these sites were unoccupied the molecule was inserted therein and its energy in the new position, U_{new}, was calculated using the same procedure as for U_{old}. Otherwise, the molecule was left in the original position. To decide whether the new molecular configuration should be accepted the probability factor $p = \min[1,\exp(-\Delta U/k_BT)]$ with $\Delta U = U_n - U_o$ and k_B being the Boltzmann constant was calculated and compared with a randomly generated number $r \in (0,1)$. If $r < p$ the new configuration was accepted; otherwise the attempt ended, leaving the molecule in the old position. The above procedure was repeated several times, using typically $5N \times 10^6$ MC steps, until equilibration of the adsorbed phase. To eliminate the risk of trapping the modeled superstructures in metastable states we used the cooling procedure[52] in which the temperature of the system was slowly decreased from 1 to 0.01 in 1000 intervals of equal length. The energies and temperatures in our model are expressed in units of ε and $|\varepsilon|/k_B$, respectively. As a single molecule **A–J** comprises six segments, for a system comprising N molecules adsorbed on the triangular lattice with side L (sites) the total number of segments is equal to $6N$ and the number of lattice sites is equal to L^2. Accordingly, the surface coverage, θ, was defined as an average number of molecular segments per lattice site, that is $6N/L^2$. The quantitative dependencies of this study are averages over ten independent systems.

3. Results and discussion

To examine the self-assembly of the tetrapod tectons we performed a series of calculations aiming at the identification of possible ordered phases occurring in the modeled systems. Most of these simulations were carried out at relatively low surface coverage, to ensure unrestricted growth of adsorbed superstructures. Moreover, for a few selected systems with bigger lattice size we additionally used the parallel tempering MC technique[54] which effectively facilitates equilibration of large molecular assemblies, especially at higher adsorbate densities (see Fig. S3, ESI†). Our MC simulations embraced one-component systems comprising molecules of **A** or the *R*-enantiomers of **B–J** and, additionally, racemic mixtures in which both enantiomers of **B–J** were present on the surface. In the following we discuss the results obtained for these two cases, collected in separate subsections.

One-component systems

Achiral tecton A. Let us start the discussion with the simplest (parent) tecton **A** bearing the interaction directions all of which are collinear with the corresponding molecular arms. Fig. 2 presents the results obtained for 1400 molecules ($\theta = 0.21$) at $T = 0.1$. As mentioned previously, this value of θ, assumed for all of the modeled systems, was carefully chosen to allow adsorbed domains grow freely and to avoid occlusion of excess molecules in the pores of the self-assembled networks.

As it can be seen in the figure, the molecules of **A** can form either the Kagome or the brickwall pattern with rhombic and square unit cells, respectively. Importantly, the connectivity of each molecule of **A** in both patterns is identical, that is each molecule of (α)**A** and (β)**A** (infinite defect-free overlayer) has four neighbors, so that the interaction energy (four bonds, 4ε) is the same. Moreover, the densities of these two patterns are very close and equal to $\rho[(\alpha)\mathbf{A}] = 0.424$ and $\rho[(\beta)\mathbf{A}] = 0.462$, respectively (see Fig. S1, ESI†). The main difference between (α)**A** and (β)**A** lies thus in the molecular arrangements which result in the formation of hexagonal (yellow) and triangular (green) pores in (α)**A** and rhombic (blue) pores in (β)**A**. The identical energetic properties of the simulated porous networks as well as their very similar densities make the occurrence of these superstructures strongly affected by entropic factors. In consequence, the coexistence of these patterns has a complex character and manifests itself in the competition between the networks shown in Fig. 1. For example, the results shown therein were obtained with a completely disordered set of adsorbed molecules whose self-assembly during gradual lowering of the temperature (from $T = 1.0$ to $T = 0.1$) resulted either in (α)**A** or in (β)**A** with the first phase being recorded much more frequently. This effect was observed also in the advanced calculations done with the parallel tempering method,[54] which showed that (α)**A** is a thermodynamically stable phase at low surface coverages (see Fig. S1, ESI†). Analysis of molecular connectivity as a function of temperature performed for the self-assembly of the Kagome and brickwall phases from Fig. 2 revealed that the formation of these two networks is characterized by very similar dependencies. This can be clearly seen in Fig. 3 in which we plotted the corresponding changes in molecular connectivity induced by the gradual lowering of temperature. The thick and thin solid lines from the left panel coincide at higher temperatures, highlighting identical self-assembly mechanisms of the Kagome and brickwall networks in this regime. Enhanced formation of both these superstructures occurs at the transition temperature equal to about 0.35, at which a steep increase in the number of fully coordinated molecules ($n = 4$) is observed. This rapid increase was preceded by a gradual decrease in the number of unbounded molecules ($n = 0$, black) which are consumed to produce single (red), double (green) and triple (orange) connections whose populations increase when the temperature approaches 0.35. At this point the occurring molecular condensation makes the molecules maximize their coordination, so that the number of tectons with n ranging from one to three rapidly drops.

As it follows from Fig. 3, after crossing the transition temperature, the curves corresponding to the Kagome and brickwall self-assembly (n = 2, 3 and 4) start to differentiate. This effect is a direct consequence of the different structural properties of the domain boundaries limiting the assemblies from Fig. 2 (see Fig. S1, ESI†). Specifically, the perimeter of the

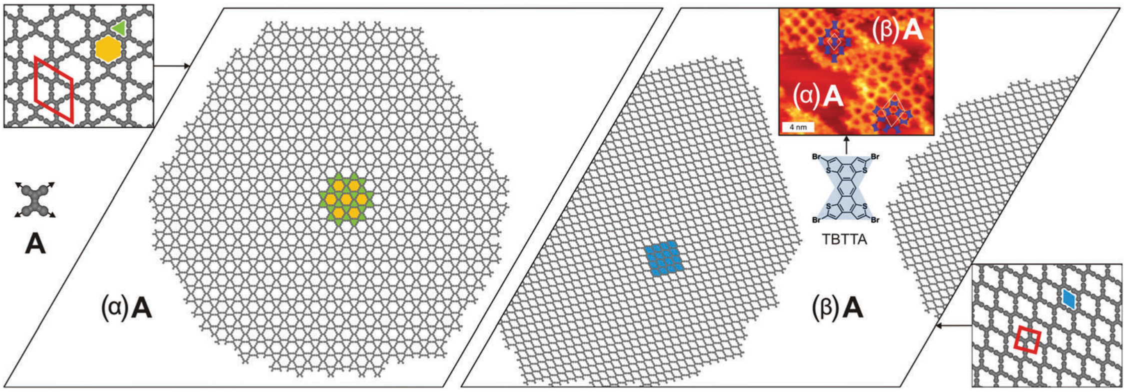

Fig. 2 Snapshots of the porous Kagome (α) and brickwall (β) phase formed by 1400 molecules of **A** (θ = 0.21) at T = 0.1. The hexagonal and triangular pores of (α)**A** and rhombic pores of (β)**A** are colored in yellow, green and blue, respectively. The red solid lines delimit the rhombic and square unit cells of the simulated structures (see the ESI†). The inset in the right panel shows the coexisting metal–organic patterns formed by the brominated tetrathienoanthracene (TBTTA) on Cu(111).[42] (Reproduced and adapted from ref. 42 with permission from the Royal Society of Chemistry.) These patterns are isostructural with (α)**A** and (β)**A**, as indicated in the STM image.

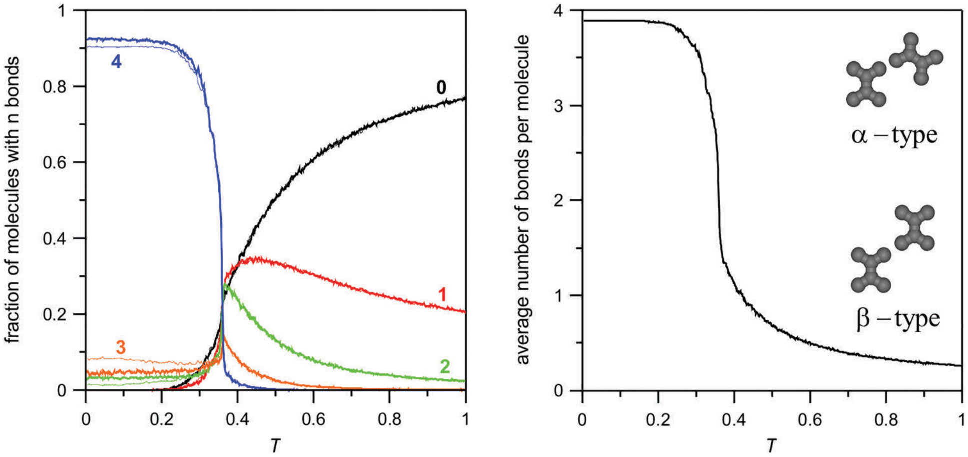

Fig. 3 Fraction of molecules with $n = 0.4$ bonds as a function of temperature (left) and average number of bonds per molecule (right) calculated for the self-assembly of the Kagome (thick lines) and brickwall (thin lines) networks comprising 1400 molecules of **A** ($\theta = 0.21$). The corresponding thin and thick solid lines from the left panel coincide fully ($n = 0, 1$) or partially ($n = 2, 3, 4$; $T > 0.35$) for the two simulated systems comprising **A**. The average functional dependencies from the right panel are identical for both network types. The insets in the right panel show the basic bimolecular structural motifs stabilizing the Kagome (α) and brickwall (β) networks.

brickwall pattern consists of straight sections in which each contributing molecule forms three bonds. The molecules with two bonds are much less frequently populated, being located mainly at vertices terminating the straight sections. On the other hand, the peripheral zone of the Kagome network comprises a larger number of molecules with $n = 2$, as compared to the brickwall pattern. These molecules ''protrude'' from the perimeter of (α)**A** and make it more corrugated. Moreover, this type of termination reduces considerably the number of molecules with three bonds. The effects discussed above are reflected in the relative position of the curves with $n = 2$, 3 and 4 (thick and thin lines) at low temperatures ($T < 0.2$) at which the domain boundaries are finally formed. In the case of the last coordination number, the Kagome network comprises a slightly larger number of fully coordinated molecules ($n = 4$) which, contrary to the brickwall pattern, can be partially exposed and contribute to the perimeter of (α)**A**. Molecules of this type are, for example, those placed between two neighboring ''spikes'' at the periphery of this network (see Fig. S1, ESI†). In consequence, the curve plotted for the Kagome self-assembly (blue thick line) lies slightly above the curve obtained for the brickwall network.

As it is demonstrated in the right panel of Fig. 3, the subtle differences in the connectivity of (α)**A** and (β)**A** observed at low temperatures vanish completely when the average number of bonds per molecule is considered. The effects associated with different populations of molecules with $n = 2$, 3 and 4 compensate for a given network resulting in the overlapping temperature dependencies shown in the right panel. Even though the average connectivities of the Kagome and brickwall networks change with temperature in the same way, the formation of each of these patterns can be easily distinguished based on the structural properties of elementary bimolecular connections occurring in (α)**A** and (β)**A**. Specifically, there are two unique α- and β-type bonding motifs which can be found exclusively in the Kagome and brickwall phase, respectively. These binding motifs, shown in the inset of Fig. 3, engage two neighboring molecules whose orientations differ by 60 degrees (α) or are identical (β). Contrary to the results from Fig. 3, the temperature dependence of the number of bonds of type α and β clearly reveals the formation of the associated networks. This is demonstrated in Fig. S2, ESI,† which shows how the different binding motifs (bonds of type α and β) contribute to the net effect (sum of bonds of type α and β) observed for the Kagome and brickwall self-assembly. Importantly, these bonding motifs are not only theoretical predictions but they are also responsible for the stabilization of diverse real molecular structures with the Kagome and brickwall morphology. The occurrence of these competing phases was observed experimentally, for example in the metal-mediated self-assembly and subsequent polymerization of brominated tetrathienoanthracene (TBTTA) on Cu(111).[42] As it is seen in the example from Fig. 2, the simulated Kagome and brickwall patterns agree well with their experimental counterparts (see the inset) which demonstrates the accurate predictive power of the proposed approach. Moreover, our theoretical findings are consistent with the experimental results obtained for a small **A**-type molecule of pyromellitic acid (PMA) adsorbed at the graphite/organic solvent interface.[55] In this example, the tetracarboxylic PMA tectons were found to form coexisting polymorphs which are structurally very similar to the Kagome and brickwall phases (α)**A** and (β)**A**. In real situations structure formation in adsorbed systems comprising organic tectons of type **A** can be affected by molecule–surface interactions and molecule–solvent interactions which can promote development of either (α)**A** or (β)**A** or their coexistence under given external conditions. The obtained results show that, even without information of this type the proposed model allows for accurate identification of possible 2D superstructures comprising **A**-type units.

Chiral tectons B–J. To test further the model we performed the simulations for the chiral tectons **B–J**, the first of which forms the three ordered phases shown in Fig. 4. In this case,

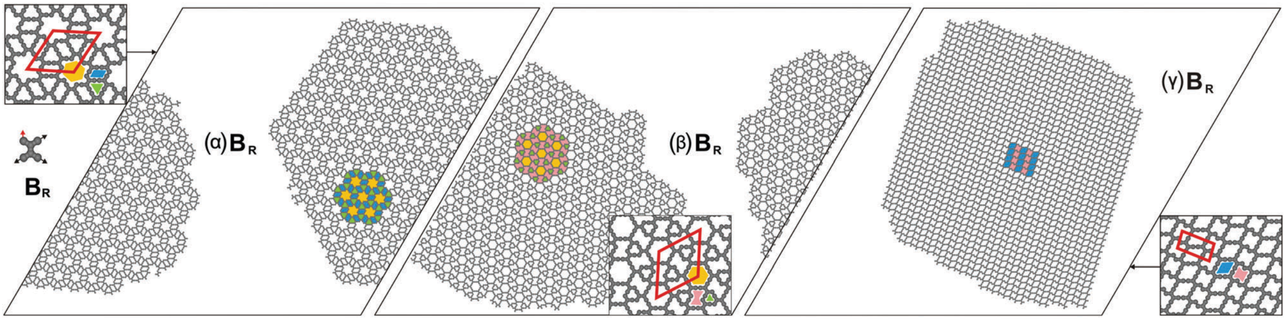

Fig. 4 Snapshots of the ordered porous phases formed by 1400 molecules of **B**(R) ($\theta = 0.21$) at $T = 0.1$. The hexagonal and triangular pores of (α)**B** and (β)**B** are marked in yellow and green while the remaining pores with a parallelogram and a less regular shape are colored in blue and pink, respectively. The red solid lines delimit the rhombic (α, β) and parallelogram (γ) unit cells of the simulated structures (see the ESI†).

modification of one interaction direction in the parent molecule **A** (red arrow) led to a much more complex phase behavior. The three ordered phases shown in the figure emerged as a result of the simulations which, like for the molecule **A**, started from entirely random spatial distribution of the molecules on the surface, at a relatively low surface coverage $\theta = 0.21$. The enantiopure assemblies comprising (α) and (β)$\mathbf{B}_{R}$ are characterized by a flower-type architecture the basic structural motif of which is the hexagonal pore (yellow) surrounded by alternating triangular (green), parallelogram (α, blue) or sandglass (β, pink) pores. The third brickwall phase (γ) observed in the simulations comprises alternating rows of pores which are parallelogram (blue) and sandglass (pink) in shape. A special property of the phases (α) and (β)$\mathbf{B}_{R}$ (infinite and defect-free) is that they are identical in terms of energy and density. Specifically, each molecule of (α) and (β)$\mathbf{B}_{R}$ interacts with four neighbors (4ε), and moreover, $\rho[(\alpha)\mathbf{B}_{R}] = \rho[(\beta)\mathbf{B}_{R}] = 0.457$. These common features make the occurrence of the polymorphs (α) and (β) strongly entropy driven and, thus, very difficult to predict under given θ and T. This refers also to higher surface coverages at which coexistence of the three phases of $\mathbf{B}_{R}$(α, β, γ) was observed in separate simulations performed for much larger systems using the parallel tempering technique[54] ($L = 480$, see Fig. S3, ESI†).

The next modification of **A**, involving one interaction direction, gives the unit **C** which revealed to be able to form the two porous networks shown in Fig. 5. A distinctive feature of the openwork phase (α)$\mathbf{C}_{R}$ is the presence of exceptionally large hexagonal pores (yellow) whose rims comprise 12 connected molecules. Like for the parent tecton **A**, this network has a Kagaome-type structure in which the triangular pores (green) surround the central hexagonal cavity. The structural similarity between (α)**A** and (α)$\mathbf{C}_{R}$ originates mainly from the fact that the latter network can be treated as an expanded version of the first one. Specifically, each rim of the large hexagonal pores of (α)$\mathbf{C}_{R}$ comprises one extra molecule, as compared to (α)**A**. These additional molecules are responsible for the formation of the small linking pores (pink), which form the

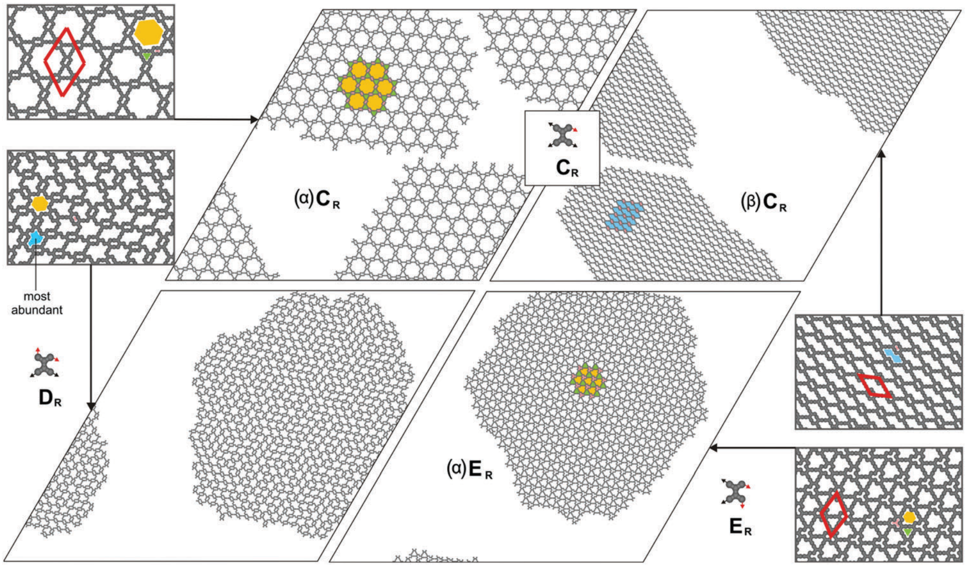

Fig. 5 Snapshots of the porous networks formed by 1400 molecules of $\mathbf{C}_{R}$–$\mathbf{E}_{R}$ ($\theta = 0.21$) at $T = 0.1$. The hexagonal and triangular pores in the periodic networks ($\mathbf{C}_{R}$, $\mathbf{E}_{R}$) are colored in yellow and green respectively. The remaining pores with less regular shapes are marked in blue (bigger) and pink (smaller). The red lines delimit the rhombic (α)($\mathbf{C}_{R}$, $\mathbf{E}_{R}$) and parallelogram (β)$\mathbf{C}_{R}$ unit cells of the simulated superstructures (see the ESI†).

vertices of the large hexagonal cavity (yellow) in (α)$\mathbf{C}_R$. A similar conclusion refers to the second, brickwall-type phase shown in the top-right part of Fig. 5. In this case the elongated parallelogram pores (blue) are formed by six molecules of $\mathbf{C}_R$, two of which, located at the opposite rims, are in excess in comparison to (α)**A**.

The next two molecules from Fig. 1, $\mathbf{D}_R$ and $\mathbf{E}_R$, were found to exhibit considerably simpler phase behavior, as compared to the cases studied so far. This observation refers to the reduced number of possible types of superstructures created by these molecules. Specifically, for each building block the simulations predicted the formation of just one porous phase. However, for the molecule $\mathbf{D}_R$ the obtained network was aperiodic with void spaces having diverse shape. The networks simulated for the building blocks $\mathbf{D}_R$ and $\mathbf{E}_R$ are shown in Fig. 5. The glassy overlayer built of the first tecton comprises nanopores of five main types (see Fig. S4, ESI†) which are randomly connected to form the continuous network with rare structural defects (partially coordinated molecules). Because of the multiple molecular arrangements producing six-membered pore rims the irregular pores shown in Fig. 5 (blue) are most abundant (∼34%) and the regular hexagonal pores (yellow) are only sparsely populated (3%). As the network formed by $\mathbf{D}_R$ is aperiodic, its density can be defined only in a statistical way. Accordingly, to estimate the average density we used ten independent system replicas and for each of them we reckoned occupied sites within a 50 × 50 rhombic fragment cut-off from the corresponding domain. The obtained value, that is the total number of segments divided by the fragment area, equals 0.465 ± 0.003. Contrary to the amorphous phase formed by $\mathbf{D}_R$, the self-assembly of the second tecton $\mathbf{E}_R$ resulted in the extended periodic network comprising nanopores of the three types shown in the inset. An interesting effect observed here is that the dichotomous self-assembly of $\mathbf{C}_R$ (phases α and β) is replaced by the one-phase formation when one interaction direction in $\mathbf{C}_R$ is modified to obtain $\mathbf{D}_R$ (bottom left) and $\mathbf{E}_R$ (bottom right).

Fig. 6 presents the results simulated for the molecule $\mathbf{F}_R$, which revealed to be the only tecton incapable of forming network structures. To understand this effect let us look at the interaction pattern encoded in $\mathbf{F}_R$. A special property of this building block is that it bears the interaction directions which are collinear on both sides of the molecule (see Fig. 1). In consequence, the self-assembly of $\mathbf{F}_R$ is highly site-specific, and occurs *via* preferential side-to-side attachment of the molecules creating the ladders shown in the left panel. The observed self-assembly scenario is the preferred one, as it offers quicker coordination of a molecule, as compared to the nucleation and growth of alternative network structures. Specifically, the propagation of the ladders is largely enhanced due to the energetically favorable simultaneous formation of two bonds between a pair of molecules. Each bond of this type has a mixed character as it engages the unlike orientation directions marked with the red and black arrows in the figure. The observed growth mechanism of the ladders is very effective, eliminating the other possible intermolecular connections involving interaction directions of the same type (black–black and red–red) which would cement the hypothetical network structure. To illustrate this in the right panel of Fig. 6 we have shown the effect of temperature on the average number of bonds of different types formed between molecules of $\mathbf{F}_R$ in the adsorbed overlayer. The curves presented in the figure clearly demonstrate the preferential formation of the ladder-type connections. To quantify this process we calculated also the average ladder length as a function of temperature and the ladder length distribution functions at different temperatures. These dependencies are shown in Fig. 7.

The obtained results demonstrate enhanced formation of longer ladder structures when the temperature drops below 0.3, which is reflected in the steep growth of the curve from the left panel. A detailed analysis of the composition of the adsorbed phase at the three temperatures indicated in the left part (colored circles) yields the different ladder-length distribution functions presented in the right part. As it can be expected, the maximum of these dependencies shifts towards lower values when the temperature increases, meaning the formation of shorter connections at elevated temperatures. Interestingly, the distributions obtained from the simulations are similar in shape to the Flory–Schulz (FS) distribution functions characterizing the

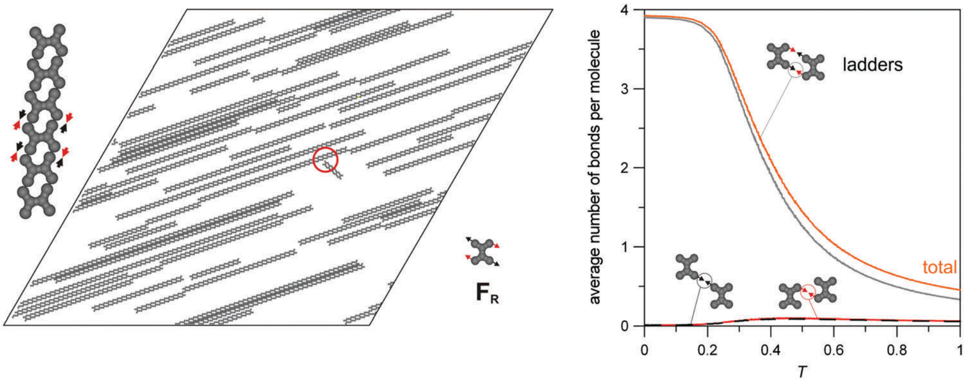

Fig. 6 Snapshot of the ladder structures formed by 1400 molecules of $\mathbf{F}_R$ (θ = 0.21) at T = 0.1 (left). The inset in the left panel shows the pairs of different interaction directions (red and black arrows) responsible for cementing the chains. The red circle indicates the configuration in which, due to the steric blockade, the shorter ladder cannot grow at one end. Influence of temperature on the average number of bonds engaging the different orientation directions (right). The insets show bimolecular configurations corresponding to the three possible combinations of the interaction directions.

step-growth polymerization. This observation made us to compare our results with the predictions of the FS statistics, that is assuming for a while that the ladder propagation occurs due to the step-growth mechanism. A detailed description of this procedure can be found in the ESI.† The predicted FS distributions (black solid lines) are in better agreement with the MC data as long as the temperature is relatively low (red and blue step curves). When the temperature increases the number of short ladder structures is considerably higher than that provided by the FS theory (green step curve). There are two main reasons which make our results different from the FS predictions. The first is that the propagation of the ladders is correlated, contrary to the ideal step-growth mechanism which treats the growing polymer chains as totally independent objects. A simple illustration of this effect in our case is the growth of a pair of ladders along directions which cross, so that further growth of one of these ladders is blocked, as seen in Fig. 6 (red circle). The second reason is that the MC moves of our algorithm allow for breaking a ladder by removing one molecule from its interior to produce two shorter structures and this process, although usually energetically not beneficial, can, nonetheless, occur at elevated temperatures. These factors are responsible for the increased population of short ladders at elevated temperatures, as compared to the FS theory. On the other hand, when the temperature decreases the agreement between the simulations and the FS approach is somewhat better and this results from the lowered chance of breaking the ladders by removal of internal molecules.

The simulations performed for the molecules **G** and **H** similarly to **C** revealed the formation of porous networks of two types (α and β). These networks are shown in Fig. 8 and the magnified fragments inserted therein present the hexagonal pores of (α)$\mathbf{G}_{\boldsymbol{R}}$ and (α)$\mathbf{H}_{\boldsymbol{R}}$ and the less regular pores in the brickwall-type structures (β)$\mathbf{G}_{\boldsymbol{R}}$ and (β)$\mathbf{H}_{\boldsymbol{R}}$. A distinctive feature of the phase (α) formed by the molecules $\mathbf{H}_{\boldsymbol{R}}$ is the occurrence of large hexagonal pores covering 67 adsorption sites each (yellow). Moreover, the rims of these pores are thicker, as compared to for example (α)**A**. The rims of $\mathbf{H}_{\boldsymbol{R}}$ comprise small (two-membered) fragments of the ladders from Fig. 6 (see the inset). Note also that the self-assembly in the overlayers comprising $\mathbf{H}_{\boldsymbol{R}}$ produces networks which are structurally similar to those created by the tecton $\mathbf{C}_{\boldsymbol{R}}$ (see Fig. 5). The presence of large pores makes the density of phase (α)$\mathbf{H}_{\boldsymbol{R}}$ considerably smaller than the density of the more compact phase (β)$\mathbf{H}_{\boldsymbol{R}}$, that is 0.355 *vs.* 0.533. A similar, although less profound, effect can be observed for the molecule $\mathbf{G}_{\boldsymbol{R}}$, for which the density of the phases (α) and (β) is equal to 0.424 and 0.495, respectively. Another interesting observation is that the brickwall phase (β)$\mathbf{G}_{\boldsymbol{R}}$ is characterized by the lowest structural complexity among the patterns shown in Fig. 8. This refers to the number of different pores which can be found in these superstructures, equal to just one for (β)$\mathbf{G}_{\boldsymbol{R}}$. This type of structural homogeneity was already observed for the brickwall phase (α) formed by the achiral tecton **A** from Fig. 2. A common feature of the molecules **A** and **G** is the C_2 symmetry which is higher compared to the tectons **C** and **H** which are also able to create brickwall-type phases. As we will show later this principle applies as well to the unit **J** having a C_2-symmetric structure.

In the case of the molecule $\mathbf{I}_{\boldsymbol{R}}$ our calculations demonstrated the possibility of creation of the three ordered porous phases shown in Fig. 9. The structure formation observed here is qualitatively similar to the one referring to the building block $\mathbf{B}_{\boldsymbol{R}}$ (compare with Fig. 4). Like for $\mathbf{B}_{\boldsymbol{R}}$, here the self-assembly produces two flower-type phases (α, β) each consisting of nanocavities of three types and the brickwall phase (γ) being a mixture of alternating rows of pores of two types. The similarity between the structures simulated for $\mathbf{B}_{\boldsymbol{R}}$ and $\mathbf{I}_{\boldsymbol{R}}$ can be attributed to the same number of collinear interaction directions (one pair) encoded in these molecules. We will come back to this property later in this section.

The 2D self-assembly in the systems comprising the tecton $\mathbf{J}_{\boldsymbol{R}}$ resulted in the two possible ordered phases shown in Fig. 10. The dichotomous structure formation observed here is qualitatively similar to those found for the units **A** and $\mathbf{G}_{\boldsymbol{R}}$. The Kagome-type

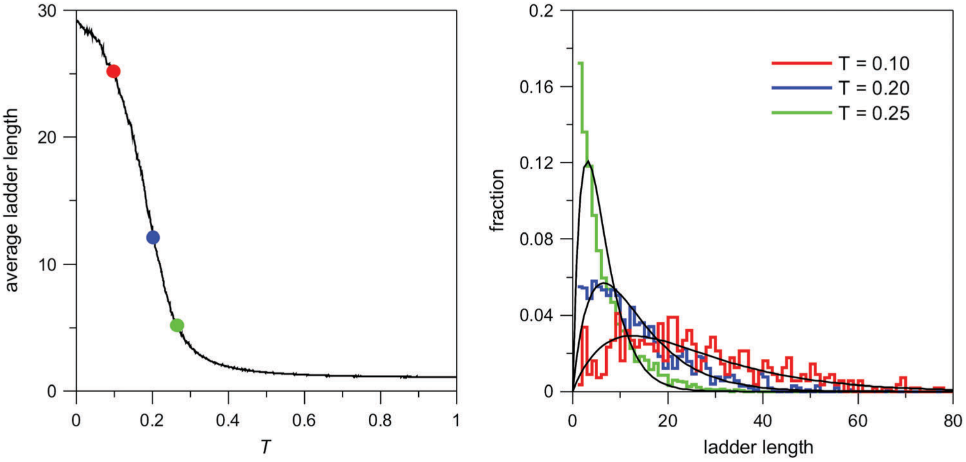

Fig. 7 Average ladder length (expressed in number of molecules) as a function of temperature (left) and distributions of the ladder length calculated for the three temperatures from the left panel: 0.1 (red), 0.2. (blue) and 0.25 (green), for 1400 molecules of $\mathbf{F}_{\boldsymbol{R}}$ (θ = 0.21). The black solid lines in the right panels are the corresponding results predicted by the Flory–Schultz theory (see the ESI†).

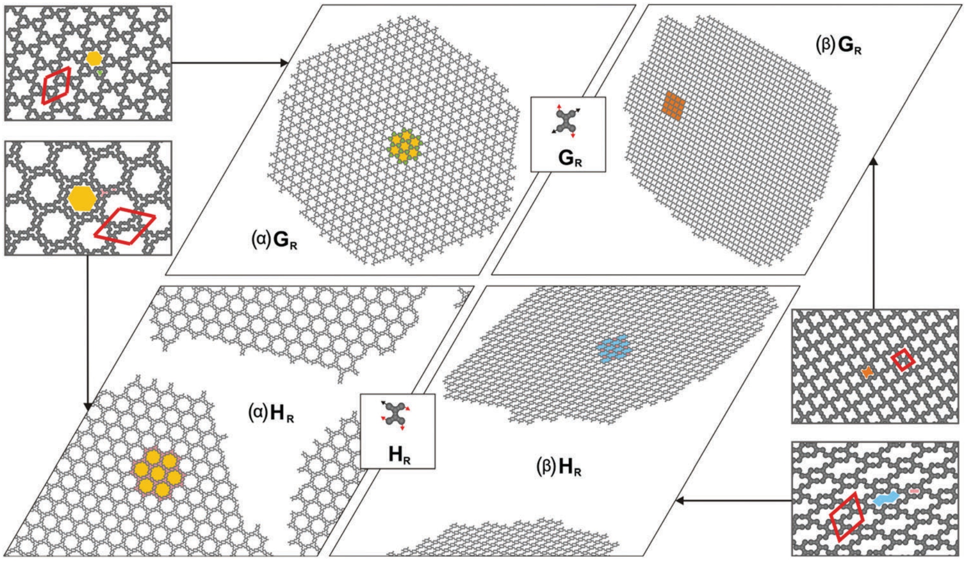

Fig. 8 Snapshots of the porous networks formed by 1400 molecules of **G**(*R*) and **H**(*R*) (θ = 0.21) at T = 0.1. The hexagonal and triangular pores in the periodic networks (α-type) are colored in yellow and green respectively. The remaining pores with less regular shapes are marked in blue and orange (bigger) and pink (smaller). The red lines delimit the rhombic (α) and parallelogram (β) unit cells of the simulated superstructures (see the ESI†).

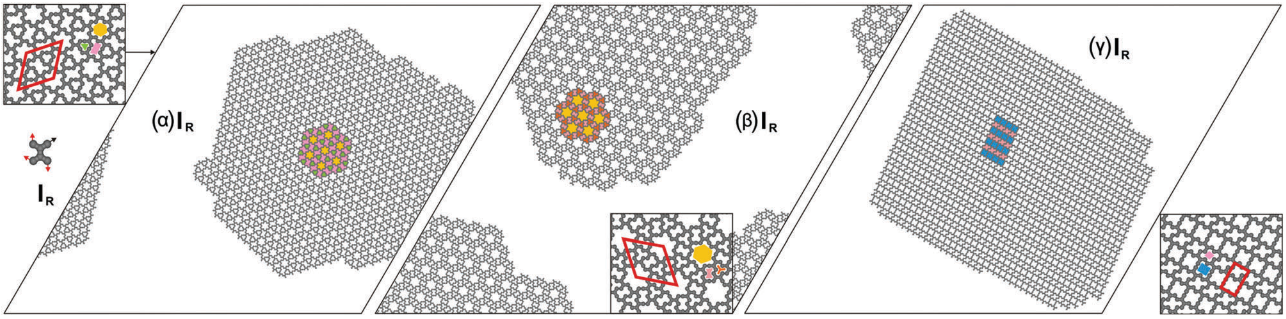

Fig. 9 Snapshots of the porous networks formed by 1400 molecules of $\mathbf{I}_{\boldsymbol{R}}$ (θ = 0.21) at T = 0.1. The hexagonal and triangular pores in the networks (α) and (β) are colored in yellow and green respectively. The remaining pores with less regular shapes are marked in blue (γ), orange and pink. The red lines delimit the rhombic (α, β) and parallelogram (γ) unit cells of the simulated superstructures (see the ESI†).

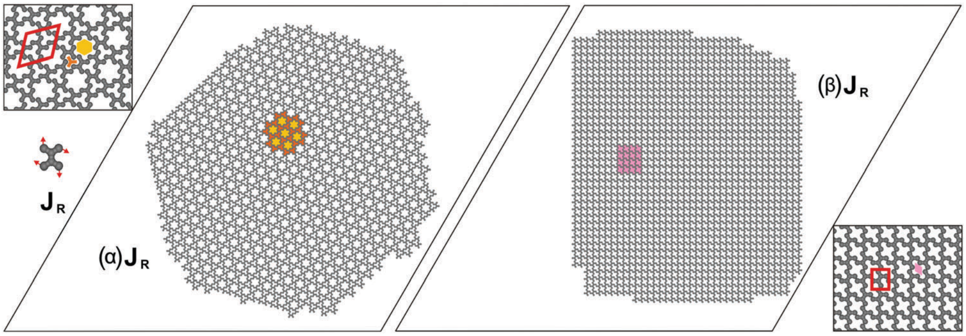

Fig. 10 Snapshots of the porous networks formed by 1400 molecules of $\mathbf{J}_{\boldsymbol{R}}$ (θ = 0.21) at T = 0.1. The hexagonal pores in the network (α) are colored in yellow. The smaller, less regular, pores in (α) and (β) are marked in orange and pink, respectively. The red lines delimit the rhombic (α) and parallelogram (γ) unit cells of the simulated superstructures (see the ESI†).

network (α)$\mathbf{J}_{\boldsymbol{R}}$ comprises pores of two types, that is the bigger hexagonal (yellow) and the smaller tripod-shaped (orange) ones. Like for **A** and $\mathbf{G}_{\boldsymbol{R}}$, the second possible brickwall phase (β)$\mathbf{J}_{\boldsymbol{R}}$ is homogeneous in terms of porosity, as it contains void spaces of one type (pink). As we mentioned previously, the dichotomous self-assembly of the units **A** and $\mathbf{G}_{\boldsymbol{R}}$ can be associated with the highest symmetry of these tectons among **A–J**. Indeed, this relationship applies also to the unit $\mathbf{J}_{\boldsymbol{R}}$ which has a symmetry center.

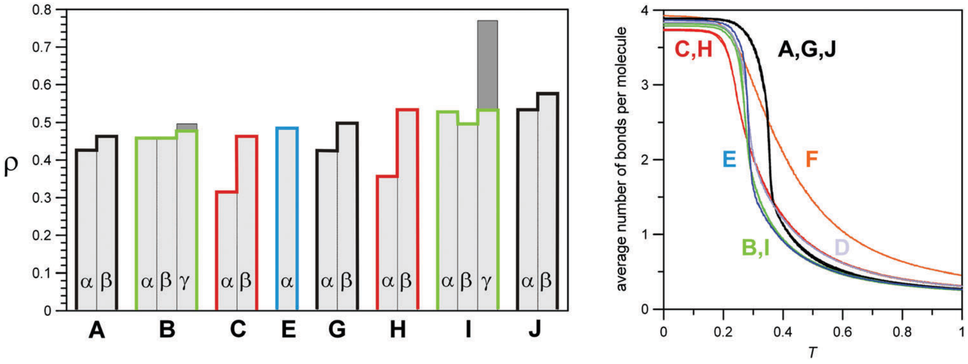

Fig. 11 (left) Density of the possible ordered phases (infinite and defect-free) formed by the molecules **A–J**. The results plotted in light and dark grey correspond to the homochiral and racemic superstructures, respectively. (right) Average number of bonds per molecule as a function of temperature calculated for the tectons **A–J** (*R*-enantiomers). The systems for which the self-assembly resulted in identical or very close temperature dependencies are represented by the same color code in both panels.

To summarize the quantitative properties of the simulated systems, in Fig. 11 we compared the densities of the different ordered porous phases formed by the molecules **A–J**. Moreover, for each tecton we calculated the average connectivity of the molecular building block as a function of temperature. These results are collected in Fig. 11 in which, for comparative purposes, we showed also the curves determined for **A** (Fig. 3) and $\mathbf{F}_R$ (Fig. 6).

In general, the densities of the ordered homochiral phases shown in the left part do not exceed 0.6, with the lowest and higher value corresponding to the network (α)$\mathbf{C}_R$ (0.313) and (β)$\mathbf{J}_R$ (0.577), respectively. The data plotted in the figure show that in most cases, the differences between the densities of the competing phases are similar and they lie within the range 0–20% (**A**, **B**, **G**, **I** and **J**). Among them there are extreme cases such as the networks (α)$\mathbf{B}_R$ and (β)$\mathbf{B}_R$ having the same density or the phases (α)$\mathbf{I}_R$ and (γ)$\mathbf{I}_R$ whose densities differ by only 1.3%. On the other hand, the largest differences are observed for the molecules $\mathbf{H}_R$ (50%) and $\mathbf{C}_R$ (36%).

As shown so far, the structure formation in the modeled enantiopure adsorbed systems differs depending on the way in which the intermolecular interactions are encoded in the parent building block. However, there are molecular features which make the mechanisms of the self-assembly of certain tectons very similar or identical. This can be clearly seen in the right part, in which we plotted the average number of bonds per molecule as a function of temperature. For example, the curves calculated for $\mathbf{A}_R$, $\mathbf{G}_R$ and $\mathbf{J}_R$ are identical, highlighting the same self-assembly scenario. These three building blocks are characterized by the highest symmetry (symmetry center) and this property is responsible for the formation of the two types of ordered phases (Kagome and brickwall) for each molecule. Moreover, the similar structures of the corresponding domain boundaries created by these tectons provide identical average connectivity. The reduced number of ways in which the molecules of $\mathbf{A}_R$, $\mathbf{G}_R$ and $\mathbf{J}_R$ can form the associated structural motifs, imposed by the high molecular symmetry, results in the sharp transition occurring at $T \approx 0.35$, which is a relatively high value as compared to the other systems. A similar effect can be observed in the dichotomous self-assembly of the units $\mathbf{C}_R$ and $\mathbf{H}_R$ which, however, lack symmetry elements. A common feature of these molecules is that they have three interaction directions which are collinear. This relatively high order of the interaction pattern facilitates the structure formation, especially due to the presence of the pair of collinear interaction directions on one side of $\mathbf{C}_R$ and $\mathbf{H}_R$. These pairs, like for the molecule $\mathbf{F}_R$, enable the formation of two bonds between two neighboring molecules. In consequence, at higher temperatures, the connectivity in the systems comprising $\mathbf{C}_R$ and $\mathbf{H}_R$ is initially larger than for $\mathbf{A}_R$, $\mathbf{G}_R$ and $\mathbf{J}_R$.

Another pair of molecules for which the corresponding temperature dependencies are identical are the $\mathbf{B}_R$ and $\mathbf{I}_R$. Each of these molecules can form three distinct porous networks (α, β and γ) with similar architectures, **B** *vs.* **I**. This common property is reflected in the overlapping green curves from the right panel. These two molecules lack symmetry elements and, moreover, they are characterized by a lower coherence of the interaction directions, as compared to $\mathbf{C}_R$ and $\mathbf{H}_R$. Specifically, $\mathbf{B}_R$ and $\mathbf{I}_R$ possess only one pair of collinear interaction directions which are located in *cis* position of the backbone. In consequence, the correct positioning of a molecule to be incorporated in the growing cluster of phases α, β and γ is more difficult as compared to the symmetric units $\mathbf{A}_R$, $\mathbf{G}_R$ and $\mathbf{J}_R$. For that reason the molecular condensation occurs at the lower temperature $T \approx 0.27$ at which the extended porous networks α, β and γ start to develop. The two remaining molecules with one pair of collinear directions, $\mathbf{D}_R$ and $\mathbf{E}_R$, exhibit a simpler phase behavior, forming just one network type each, but the corresponding temperature dependencies are partially different. In the case of the first molecule, the presence of the collinear interaction directions on one side of the backbone, like for $\mathbf{C}_R$ and $\mathbf{H}_R$, results in the creation of double-bonded bi-molecular motifs. This effect is reflected in the identical shape of the corresponding curves ($\mathbf{C}_R$, $\mathbf{H}_R$ and $\mathbf{D}_R$) at high and moderate temperatures, $T > 0.3$. On the other hand, for the molecule $\mathbf{E}_R$ which lacks this special pair of interaction directions, at higher temperatures $T > 0.6$, the curve plotted in Fig. 11 is placed below the overlapping curves obtained for $\mathbf{C}_R$, $\mathbf{H}_R$ and $\mathbf{D}_R$. Moreover, in this temperature regime, the dependency calculated for $\mathbf{E}_R$ is identical to those obtained for the molecules which do not bear the pair of parallel interaction directions (**A**$_R$, **B**$_R$, **G**$_R$, **I**$_R$ and **J**$_R$). On the other hand, at low temperatures, the common effect of the reduced number of collinear interaction directions can be clearly seen when looking at the shapes of the curves drawn for **B**$_R$, **D**$_R$, **E**$_R$ and **I**$_R$ which are very similar for $T < 0.27$.

The markedly different shape of temperature dependence obtained for the molecule **F**$_R$ is a clear manifestation of the collinear effect of encoded interaction directions. Even though this tecton is centrosymmetric like **A**$_R$, **G**$_R$ and **J**$_R$, the particular parallel alignment of the four interaction directions makes it behave in a peculiar way. Specifically, the obtained temperature dependence is much less steep, as compared to the remaining curves. A similar effect can be observed for those molecules which have one pair of collinear interaction directions on one side of the backbone, that is **C**$_R$, **H**$_R$ and **D**$_R$. This observation indicates that, in general, the presence of the collinear interaction directions on one side is a factor which smoothes the temperature dependence of the average molecular connectivity in the modeled systems. As mentioned previously, this effect originates mainly from the gradual formation of double bonds between a pair of molecules starting yet at high temperatures.

In summary, the results of this section demonstrate that those tetrapod molecules which are highly symmetrical in terms of the interaction directions are able to undergo the dichotomous self-assembly producing the Kagome and brickwall-type porous networks. Moreover this high symmetry is responsible for the occurrence of the rapid structural transition (condensation) at elevated temperatures. The second important factor which affects the structure formation in the modeled systems is the number of collinear interaction directions in the molecule, especially the number of such directions on one side of the backbone. The tetratopic molecules which have the same number of collinear directions were found to behave in a similar way, including **C**$_R$ and **H**$_R$ with three collinear directions and two possible phases and **B**$_R$ and **I**$_R$ with two collinear directions and three possible phases. The reduced symmetry of the interaction pattern inherent to these molecules is also the source of the shift of the transition temperature towards lower values. This, however, refers to those asymmetric molecules which do not bear the pair of parallel interaction directions on one side. The presence of such a pair in the building block results in much less rapid changes in the intermolecular connectivity which are induced by decreasing temperature. The self-assembly of molecules having the pair of parallel interaction directions on one side produces different superstructures whose architecture is dependent on the two remaining interaction directions. Nevertheless, at high temperatures the self-assembly of these building blocks is characterized by the average connectivity functions of the same shape.

Racemic mixtures

To identify new 2D structures which can spontaneously form in mixed systems comprising both enantiomers of **B–J** we performed the simulations for the corresponding racemic overlayers. Emergence of such structures was observed only for molecules **B**, **C**, **G** and **I**, as shown in Fig. 12. We emphasize that the pattern formation in the mixed systems was in general more complex than in the corresponding one-component assemblies, so that the new racemic phases were often found to coexist with the homochiral domains. In the following we focus on the selected examples in which the new racemic structures were found to engage all of the adsorbed molecules. Specifically, periodic mixed molecular patterns were created by the tectons **B** and **I** while the self-assembly of the two remaining units resulted in structures lacking long range order, nonetheless providing maximal coordination for both enantiomers of **C** and **G**. The porous

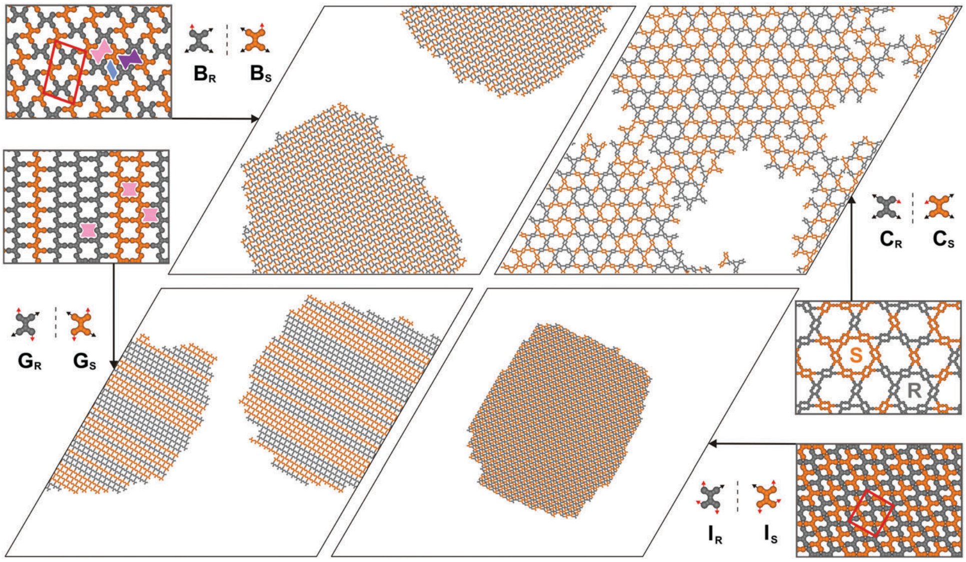

Fig. 12 Snapshots of the racemic overlayers comprising 1400 molecules of **B**, **C**, **G** and **I** (700*R* + 700*S*, θ = 0.21) simulated at T = 0.1. The homochiral hexagonal pores surrounded by the molecules of **C**$_R$ and **C**$_S$ are marked with *R* and *S*, respectively. The smaller, less regular, pores are colored in orange, pink and blue. The red lines delimit the rhombic (**B**) and rectangular (**I**) unit cells of the corresponding periodic superstructures (see the ESI†).

networks formed by *rac*-**B** can be viewed as a combination of alternating rows of the enantiomers $\mathbf{B}_{\boldsymbol{R}}$ (grey) and $\mathbf{B}_{\boldsymbol{S}}$ (orange) connected in such a way that pores of three types can be distinguished (see the inset). Interestingly, even though the racemic phase **B** is structurally the closest to the brickwall pattern (γ)$\mathbf{B}_{\boldsymbol{R}}$ none of the pore types occurring in that homochiral system is inherited by the racemic pattern. The similar brickwall structure of *rac*-**B** and (γ)$\mathbf{B}_{\boldsymbol{R}}$ results in close densities of these phases, that is 0.495 and 0.478, respectively. This means only 3.5% increase in packing density when both enantiomers of **B** are at play. A significantly larger increase in the packing density can be observed in the case of the tecton **I**, that is from 0.533 to 0.770 (44% increase). The obtained racemic phase **I** comprises small nanovoids covering one and two lattice sites exclusively and, thus, it is characterized by the highest packing density among the patterns of this study.

In the case of the partially ordered racemic patterns formed by **G** and **C** the self-assembly produced extended adsorbed assemblies in which new structural motifs coexist with the motifs inherited from the corresponding homochiral superstructures. For the first tecton, **G**, the mixed structure shown in Fig. 12 is an assembly of homochiral stripes of random width which are fully connected by the side *R*–*S* interactions. The local structure of the striped domains is identical to that of the enantiopure pattern (γ)$\mathbf{G}_{\boldsymbol{R}}$ or its mirror-image (γ)$\mathbf{G}_{\boldsymbol{S}}$, so that the shape of the chiral pores is preserved. A new type of pores appears at the boundary of the contacting domains built of $\mathbf{G}_{\boldsymbol{R}}$ and $\mathbf{G}_{\boldsymbol{S}}$. However, these achiral nanovoids are very similar in shape to the pores observed previously in the homochiral networks. For the second molecule **C**, the mixing of the new and old (homochiral) motifs is much more intense. The resulting porous network comprises large hexagonal pores whose rims are built of differently sequenced enantiomers $\mathbf{C}_{\boldsymbol{R}}$ and $\mathbf{C}_{\boldsymbol{S}}$. Depending on the enantiomeric composition of this sequence, the regular hexagonal pores (homochiral, (α)$\mathbf{C}_{\boldsymbol{R}}$ and (α)$\mathbf{C}_{\boldsymbol{S}}$) or new nanovoids with lower symmetry (mixed) are formed.

The different self-assembly outcome observed for the racemic systems was the chiral segregation producing well-separated homochiral structures. Examples of such structures are shown in Fig. 13 for the tectons **D**, **E**, **F** and **H**. An interesting observation here is the chiral resolution occurring for the tecton **D**. This tecton, when in homochiral overlayers, is able to create diversified connections resulting in the disordered porous network shown in Fig. 5. As it can be expected this property should be transmitted to the racemic system, so that a mixed continuous superstructure should be formed. As our simulations demonstrated, this is not true and the particular interaction directions encoded in $\mathbf{D}_{\boldsymbol{R}}$ revealed to be not compatible with those of $\mathbf{D}_{\boldsymbol{S}}$, so that these enantiomers could not connect in a way enabling the formation of mixed porous networks. A similar effect was observed also for the remaining molecules which formed either mirror-image porous networks (**E**, (α)**H**) or homochiral ladders comprising $\mathbf{F}_{\boldsymbol{R}}$ and $\mathbf{F}_{\boldsymbol{S}}$. In the last example, the self-sorting producing the homochiral ladders is similar to the effect simulated previously for the functional tripod molecules[52] and observed very recently in the experimental studies on the metal-mediated self-assembly of terpyridines on Au(111).[54]

To highlight the differences in the self-assembly mechanisms resulting in racemic mixing and chiral segregation in Fig. 14 we have shown the effect of temperature on the number of intermolecular bonds between the adsorbed enantiomers of **C** and **D**, including homochiral *R*–*R* and *S*–*S* and heterochiral *R*–*S* connections. The last parameter is especially important, as it measures directly the extent of chiral segregation in the modeled racemic assemblies.

From Fig. 14 it follows that, at low temperatures ($T < 0.1$), the total number of bonds in the compared simulated systems is nearly the same, being equal to about 2500 for **C** and 2575 for **D**. This means that, on average, a molecule each of **C** and **D** forms 3.57 and 3.68 connections with its neighbors, respectively. The obtained values, both close to 4, indicate the formation of compact domains with a minimal number of peripheral

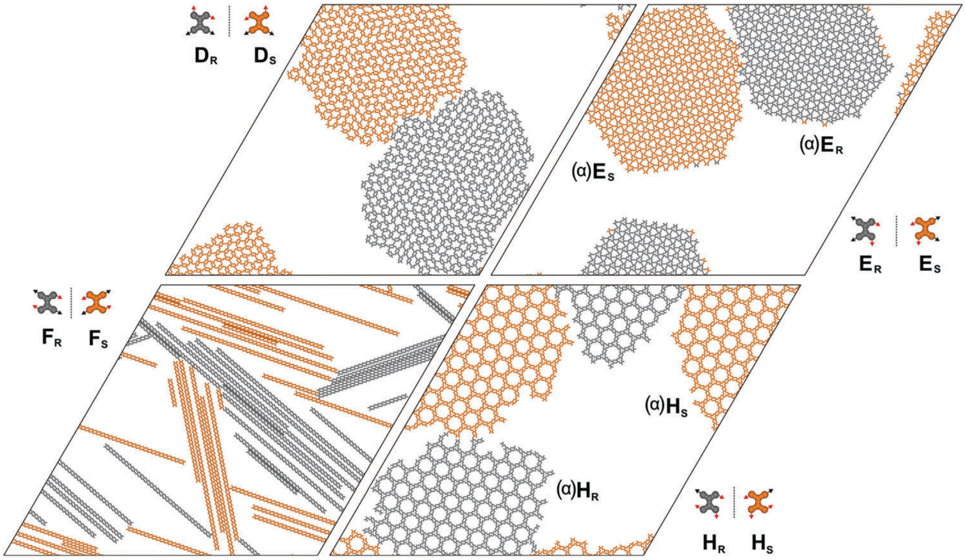

Fig. 13 Snapshots of the racemic overlayers comprising 1400 molecules of **D**, **E**, **F** and **H** (700*R* + 700*S*, θ = 0.21) simulated at T = 0.1.

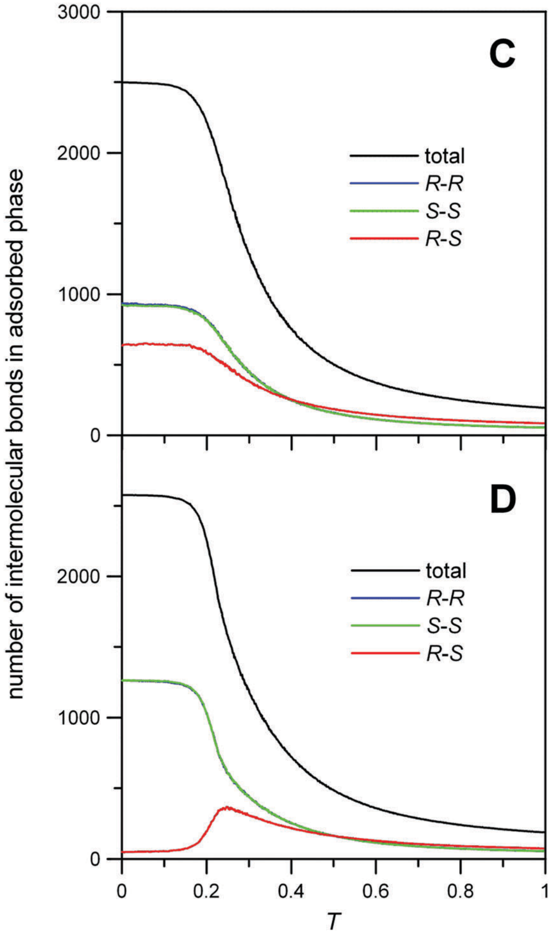

Fig. 14 Effect of temperature on the number of bonds of different types calculated for the racemic overlayers comprising 1400 molecules of **C** and **D** (700*R* + 700*S*, θ = 0.21).

undercoordinated molecules. Interestingly, the structure of the domain boundaries observed for the two types of phase behavior (mixing *vs.* segregation) has a special effect on the contact values of the black curves ($T \to 0$). Specifically, for the racemic mixing the formation of one *rac*-**C** domain, instead of two separated homochiral ones, leads to the lowering of the domain perimeter and thus it is energetically beneficial. In consequence, the number of unsaturated peripheral molecules is minimized. The chiral resolution observed for **D** should be, thus, characterized by a larger number of peripheral molecules. This is true but taking into account the connectivity of the peripheral molecules of *rac*-**C** and $\mathbf{D}_R$ and $\mathbf{D}_S$ it turns out that in the first case usually two molecular arms are engaged in the domain formation while in the second case three arms take part when located at the domain perimeter. This effect is responsible for the unusual slightly larger total molecular coordination (2500 for **C** *vs.* 2575 for **D**) in the system **D** in which the chiral resolution occurs. As mentioned previously, a measure of this process is the number of *R*–*S* connections which is represented by the red curves in Fig. 14. In the case of the system comprising *rac*-**C** we can observe a continuous increase in the number of *R*–*S* connections with decreasing temperature, reaching about 637 when T goes to zero. This value corresponds to about 25% heterochiral bonds in the systems which is comparable to the value obtained for the homochiral bonds, that is about 37% for *R*–*R* and *S*–*S*.

A completely different tendency can be seen in the case of *rac*-**D**. Here, the number of *R*–*S* connections initially increases with decreasing temperature, but when T exceeds 0.24 a rapid drop, down to about 50, occurs. The fraction of heterochiral bonds at this temperature is equal to only 2% and this residual value results from the interactions between peripheral molecules of contacting extended domains $\mathbf{D}_R$ and $\mathbf{D}_S$. The common initial increase of the number of *R*–*S* connections with temperature, observed for **C** and **D**, originates from gradual random nucleation occurring in these systems. When the temperature is sufficiently low the extended superstructures are finally formed which are either the mixed **C** domain or the homochiral **D**-domains. At these low threshold temperatures the self-sorting (**D**) or mixing (**C**) mechanism fully reveals dictating the subsequent structure formation.

The results of our MC simulations performed for the racemic mixtures show that the prediction of the structure–property relationship for these systems is much more difficult, as compared to the enantiopure overlayers. In particular, based just on the interaction directions encoded in a given tetrapod tecton, without the simulations, it would be hard to determine whether the molecule prefers to segregate or to form racemic superstructures when adsorbed on a solid substrate. As it was demonstrated, unlike for the one-component systems, there are no key molecular features which predestinate a given building block to create superstructures having certain architectures (here mixed and chirality-resolved domains). For example, the same number of collinear interaction directions which was found to be responsible for the similar self-assembly of such molecules as $\mathbf{C}_R$ and $\mathbf{H}_R$ revealed to be no longer a decisive factor, and these molecules behaved in a completely different way when in the racemic mixture. In this context, the proposed MC simulation approach appears to be a useful method which enables determination and classification of possible supramolecular structures formed by the tetrapod tectons with differently encoded interactions. In real systems, this task would require a series of test experiments with appropriately synthesized probe building blocks. Our computational investigations can facilitate this research, as they provide hints on how to design such blocks to create adsorbed structures with desired morphology.

4. Conclusions

The results from our theoretical studies demonstrate that the directionality of the interactions encoded in the tetrapod building blocks plays an important role in the 2D supramolecular structure formation. From the simulations performed for the different structural units **A–J** it follows that the majority of these tectons are able to create extended porous patterns comprising flower-type and brickwall motifs. Formation of such structures, predicted with the basic unit **A**, agrees well with the corresponding experimental results obtained with brominated tetrathienoanthracene – a molecule with **A**-type directionality of metallo-organic bonds. As it was shown, further suitable manipulation of the interaction scheme assigned to the molecular backbone 〈〉–〈〉 allowed for the creation of new adsorbed structures including ladders and networks with nanocavities of diversified shape and size. In particular, one factor which was found to be responsible for the similar structure formation in the enantiopure adsorbed systems comprising different tectons was the number of collinear interaction directions. As the modeled molecules (except **A**) are chiral in terms of the interaction directions, the complexity of homochiral 2D structures was inherited and often amplified in the associated racemic assemblies. Specifically, the calculations performed for the racemic overlayers revealed the formation of mixed crystals (**B**, **C**, **G**, **I**) while for the remaining tectons chiral resolution was possible, producing enantiopure domains. However, for the racemic systems no simple relationship between functionality of the building block and pattern formation was found, highlighting the useful role of MC calculations in predicting the self-assembly. The obtained superstructures are classified, described and collected in Table S1 (ESI†) which can serve as a small guide for selecting the proper tetrapod tecton.

The insights from our MC modeling can be helpful in designing new molecular building blocks able to form 2D superstructures with predefined morphology and functionality. The hints on the structure–property relationship outlined in this study can facilitate synthesis of these tectons, for example, indicating where to introduce functional groups (active centers) providing directional bonding. Our predictions can be also relevant to chiral self-assembly, as they distinguish between molecular building blocks able to create 2D racemic crystals and those blocks which undergo chiral resolution. The principles of molecular organization found with our theoretical approach are also of potential application in the surface-assisted polymerization reactions, in which the position of halogen atoms in a monomer often dictates connectivity of the resulting, covalently bonded, polymeric superstructure.

Conflicts of interest

There are no conflicts to declare.

Acknowledgements

This work was supported by the National Science Centre, Poland research grant 2015/17/B/ST4/03616.

References

1 A. Kühnle, Self-assembly of organic molecules at metal surfaces, *Curr. Opin. Colloid Interface Sci.*, 2009, **14**, 157–168.

2 S. De Feyter and F. C. De Schryver, *Chem. Soc. Rev.*, 2003, **32**, 139–150.

3 P. Gambardella, S. Stepanow, A. Dmitriev, J. Honolka, F. M. de Groot, M. Lingenfelder, S. Sen Gupta, D. D. Sarma, P. Bencok, S. Stanescu, S. Clair, S. Pons, N. Lin, A. P. Seitsonen, H. Brune, J. V. Barth and K. Kern, *Nat. Mater.*, 2009, **8**, 189–193.

4 M. Gobbi, S. Bonacchi, J. X. Lian, Y. Liu, X. Y. Wang, M. A. Stoeckel, M. A. Squillaci, G. D'Avino, A. Narita, K. Müllen, X. Feng, Y. Olivier, D. Beljonne, P. Samorì and E. Orgiu, *Nat. Commun.*, 2017, **8**, 14767.

5 X. Zhang, Q. Zeng and C. Wang, *RSC Adv.*, 2013, **3**, 11351–11366.

6 J. M. Gottfried, *Surf. Sci. Rep.*, 2015, **70**, 259–379.

7 J. A. A. W. Elemans, R. van Hameren, R. J. M. Nolte and A. E. Rowan, *Adv. Mater.*, 2006, **18**, 1251–1266.

8 T. Kudernac, S. Lei, J. A. A. W. Elemans and S. De Feyter, *Chem. Soc. Rev.*, 2009, **38**, 402–421.

9 J. Y. Yue, M. Markoulides, A. C. Regan, S. Y. Li, N. Chronakis, A. Gourdon, T. Chen, H. J. Yan and D. Wang, *Chem. Commun.*, 2017, **53**, 428–431.

10 J. Teyssandier, S. De Feyter and K. S. Mali, *Chem. Commun.*, 2016, **52**, 11465–11487.

11 S. Stepanow, M. Lingenfelder, A. Dmitriev, H. Spillmann, E. Delvigne, N. Lin, X. Deng, C. Cai, J. V. Barth and K. Kern, *Nat. Mater.*, 2004, **3**, 229–233.

12 N. Lin, S. Stepanow, F. Vidal, J. V. Barth and K. Kern, *Chem. Commun.*, 2005, 1681–1683.

13 D. Kühne, F. Klappenberger, R. Decker, U. Schlickum, H. Brune, S. Klyatskaya, M. Ruben and J. V. Barth, *J. Phys. Chem. C*, 2009, **113**, 17851–17859.

14 S. Ahn, C. N. Morrison and A. J. Matzger, *J. Am. Chem. Soc.*, 2009, **131**, 7946–7947.

15 K. Miyake, Y. Hori, T. Ikeda, M. Asakawa, T. Shimizu and S. Sasaki, *Langmuir*, 2008, **24**, 4708–4714.

16 A. Langner, S. L. Tait, N. Lin, C. Rajadurai, M. Ruben and K. Kern, *Proc. Natl. Acad. Sci. U. S. A.*, 2007, **104**, 17927–17930.

17 A. Ciesielski, P. J. Szabelski, W. Rżysko, A. Cadeddu, T. R. Cook, P. J. Stang and P. Samorì, *J. Am. Chem. Soc.*, 2013, **135**, 6942–6950.

18 F. Silly, *J. Phys. Chem. C*, 2017, **121**, 10413–10418.

19 M. Lackinger and W. M. Heckl, *Langmuir*, 2009, **25**, 11307–11321.

20 J. F. Dienstmaier, K. Mahata, H. Walch, W. M. Heckl, M. Schmittel and M. Lackinger, *Langmuir*, 2010, **26**, 10708–10716.

21 R. A. Barnard, A. Dutta, J. K. Schnobrich, C. N. Morrison, S. Ahn and A. J. Matzger, *Chem. – Eur. J.*, 2015, **21**, 5954–5961.

22 J. Adisoejoso, K. Tahara, S. Lei, P. Szabelski, W. Rżysko, K. Inukai, M. O. Blunt, Y. Tobe and S. De Feyter, *ACS Nano*, 2012, **6**, 897–903.

23 S. Vijayaraghavan, D. Écija, W. Auwärter, S. Joshi, K. Seufert, M. Drach, D. Nieckarz, P. Szabelski, C. Aurisicchio, D. Bonifazi and J. V. Barth, *Chem. – Eur. J.*, 2013, **19**, 14143–14150.

24 M. El Garah, A. Dianat, A. Cadeddu, R. Gutierrez, M. Cecchini, T. R. Cook, A. Ciesielski, P. J. Stang, G. Cuniberti and P. Samorì, *Small*, 2016, **12**, 343–350.

25 Z. Shi, J. Liu, T. Lin, F. Xia, P. N. Liu and N. Lin, *J. Am. Chem. Soc.*, 2011, **133**, 6150–6153.

26 Z. Shi, T. Lin, J. Liu, T. Lin, P. N. Liu and N. Lin, *CrystEngComm*, 2011, **13**, 5532–5534.

27 M. Treiter, C. A. Pignedoli, T. Laino, R. Rieger, K. Müllen, D. Passerone and R. Fasel, *Nat. Chem.*, 2011, **3**, 61–67.

28 A. Basagni, F. Sedona, C. A. Pignedoli, M. Cattelan, L. Nicolas, M. Casarin and M. Sambi, *J. Am. Chem. Soc.*, 2015, **137**, 1802–1808.

29 C. Steiner, J. Gebhardt, M. Ammon, Z. Yang, A. Heidenreich, N. Hammer, A. Görling, M. Kivala and S. Maier, *Nat. Commun.*, 2017, **8**, 14765.

30 U. Schlickum, R. Decker, F. Klappenberger, G. Zoppellaro, S. Klyatskaya, M. Ruben, I. Silanes, A. Arnau, K. Kern, H. Brune and J. V. Barth, *Nano Lett.*, 2007, **7**, 3813–3817.

31 N. Li, X. Zhang, G. C. Gu, H. Wang, D. Nieckarz, P. Szabelski, Y. He, Y. Wanga, J. T. Lü, H. Tang, L. M. Peng, S. M. Hou, K. Wu and Y. F. Wang, *Chin. Chem. Lett.*, 2015, **26**, 1198–1202.

32 M. Ammon, T. Sander and S. Maier, *J. Am. Chem. Soc.*, 2017, **139**, 12976–12984.

33 H. Bertrand, F. Silly, M. P. Teulade-Fichou, L. Tortech and D. Fichou, *Chem. Commun.*, 2011, **47**, 10091–10093.

34 M. El Garah, A. Ciesielski, N. Marets, V. Bulach, M. W. Hosseini and P. Samorì, *Chem. Commun.*, 2014, **50**, 12250–12253.

35 J. Adisoejoso, Y. Li, J. Liu, P. N. Liu and N. Lin, *J. Am. Chem. Soc.*, 2012, **134**, 18526–18529.

36 F. Bischoff, Y. He, K. Seufert, D. Stassen, D. Bonifazi, J. V. Barth and W. Auwärter, *Chem. – Eur. J.*, 2016, **22**, 15298–15306.

37 L. Grill, M. Dyer, L. Lafferentz, M. Persson, M. V. Peters and S. Hecht, *Nat. Nanotechnol.*, 2007, **2**, 687–691.

38 T. Lin, X. S. Shang, J. Adisoejoso, P. N. Liu and N. Lin, *J. Am. Chem. Soc.*, 2013, **135**, 3576–3582.

39 M. O. Blunt, J. C. Russell, M. del, C. Giménez-López, J. P. Garrahan, X. Lin, M. Schröder, N. R. Champness and P. H. Beton, *Science*, 2008, **322**, 1077–1081.

40 H. Zhou, H. Dang, J. H. Yi, A. Nanci, A. Rochefort and J. D. Wuest, *J. Am. Chem. Soc.*, 2007, **129**, 13774–13775.

41 J. Eichhorn, D. Nieckarz, O. Ochs, D. Samanta, M. Schmittel, P. J. Szableski and M. Lackinger, *ACS Nano*, 2014, **8**, 7880–7889.

42 R. Gutzler, L. Cardenaz, J. L. Duffin, M. El Garah, L. E. Dinca, C. E. Szakacs, C. Fu, M. Gallagher, M. Vondráček, M. Rybachuk, D. F. Perepichka and F. Rosei, *Nanoscale*, 2014, **5**, 2660–2668.

43 P. Iavicoli, H. Xu, L. N. Feldborg, M. Linares, M. Paradinas, S. Stafström, C. Ocal, Be. Nieto-Ortega, J. Casado, J. T. López Navarrete, R. Lazzaroni, S. De Feyter and D. B. Amabilino, *J. Am. Chem. Soc.*, 2010, **132**, 9350–9362.

44 C. A. Palma, P. Samorì and M. Cecchini, *J. Am. Chem. Soc.*, 2010, **132**, 17880–17885.

45 G. Copie, Y. Makoudi, C. Krzeminski, F. Chérioux, F. Palmino, S. Lamare, B. Grandidier and F. Cleri, *J. Phys. Chem. C*, 2014, **118**, 12817–12825.

46 C. R. L. Chapman, E. C. M. Ting, A. Kereszti and I. Paci, *J. Phys. Chem. C*, 2013, **117**, 19426–19435.

47 T. Misiūnas and E. E. Tornau, *J. Phys. Chem. B*, 2012, **116**, 2472–2482.

48 V. A. Gorbunov, S. S. Akimenko and A. V. Myshlyavtsev, *Phys. Chem. Chem. Phys.*, 2017, **19**, 17111–17120.

49 T. J. Roussel and L. F. Vega, *J. Chem. Theory Comput.*, 2013, **9**, 2161–2169.

50 Y. Li and N. Lin, *Phys. Rev. B: Condens. Matter Mater. Phys.*, 2011, **84**, 125418.

51 A. Kasperski, W. Rżysko and P. Szabelski, *Appl. Surf. Sci.*, 2016, **389**, 378–386.

52 P. Szabelski, W. Rżysko and D. Nieckarz, *J. Phys. Chem. C*, 2016, **120**, 13139–13147.

53 Y. P. Mo, X. H. Liu and D. Wang, *ACS Nano*, 2017, **11**, 11694–11700.

54 D. Frenkel and B. Smit, *Understanding Molecular Simulation: From Algorithms to Applications*, Academic Press, New York, 2002.

55 G. M. Florio, K. A. Stiso and J. S. Campanelli, *J. Phys. Chem. C*, 2012, **116**, 18160–18174.